Available online at www.sciencedirect.com
ScienceDirect
Journal of Computational Physics 227 (2008) 4038–4062
JOURNAL OF COMPUTATIONAL PHYSICS
www.elsevier.com/locate/jcp

A finite difference approach with velocity interfacial conditions for multiscale computations of crystalline solids

Shaoqiang Tang *

LTCS, Department of Mechanics and Aerospace Engineering, College of Engineering, and Center for Applied Physics and Technology, Peking University, Beijing 100871, PR China

Received 6 June 2006; received in revised form 7 October 2007; accepted 13 December 2007
Available online 23 December 2007

Abstract

We propose a class of velocity interfacial conditions and formulate a finite difference approach for multiscale computations of crystalline solids with relatively strong nonlinearity and large deformation. Full atomistic computations are performed in a selected small subdomain only. With a coarse grid cast over the whole domain and the coarse scale dynamics computed by finite difference schemes, we perform a fast average of the fine scale solution in the atomistic subdomain to force agreement between scales. During each coarse scale time step, we adopt a linear wave approximation around the interface, with the wave speed updated using the coarse grid information. We then develop a class of velocity interfacial conditions with different order of accuracy. The interfacial conditions are straightforward to formulate, easy to implement, and effective for reflection reduction in crystalline solids with strong nonlinearity. The nice features are demonstrated through numerical tests.

Keywords: Multiscale method; Interfacial condition; Finite difference; Nonlinearity

1. Introduction

With the increasing importance of modeling nanoscale structures in science and engineering, there is an urgent need to develop novel multiscale computational methods that are accurate and efficient [6]. These methods may greatly broaden the range of spatial and temporal scales for simulations, and substantiate the understanding on physics for numerous systems, e.g. [18,20,22]. In the last decade, many multiscale computational methods have been developed to model materials, including the quasicontinuum method which has been successful in simulating static and quasi-static problems [17,26], the coarse-grained molecular dynamics [24], the bridging scale method [31], the "macroscopic, atomistic, ab initio dynamics" [4], and the perfectly matched multiscale simulations [30] to simulate the dynamics. A comprehensive survey may be found in [16].

* Tel.: +86 10 62755410; fax: +86 10 62757427.
E-mail address: maotang@pku.edu.cn

0021-9991/$ - see front matter © 2007 Elsevier Inc. All rights reserved.
doi:10.1016/j.jcp.2007.12.012

We consider atomistic dynamics for crystalline solids governed by the Newton laws. Same as in the quasicontinuum method, the atomistic description is regarded as the "exact" model of material behavior [17]. In a multiscale computation, the atomistic dynamics are fully resolved only in a selected localized subdomain, where the fine scale description is necessary to model the underlying physics properly. A coarse grid representation is adopted away from there. In this manner, one reduces the degree of freedom, and hence the computing load considerably.

However, for lattices with relatively strong nonlinearity and large deformation, the accuracy of existing concurrent multiscale methods are quite limited. Either the coarse grid wave propagations are not well captured, or reflections occur in the fine scale. The major challenge is an *accurate and efficient passage of information between the two scales*.

There are two aspects for information exchange. First, one supplies the fine scale information to the coarse scale. Most aforementioned multiscale methods adopt a finite element approach in the coarse scale [26,30,31]. For a multiscale method that uses a handshaking region, the fine scale information is typically passed to the coarse scale through a weighted average in the mixed Hamiltonian or Lagrangian [1,4,14]. In our approach, we cast a finite difference grid over the whole computing domain, and adopt a coarse grid scheme designed by a matching differential operator method [28]. The scheme is explicit, and no algebraic system needs to be solved. In addition, the finite difference approach is advantageous in capturing the features of wave propagation. Noticing that solutions exist at both the coarse and fine scales over the atomistic subdomain, we average the fine scale solution for reassigning the coarse grid values [27,28]. A fast and accurate averaging technique is presented in Section 2.1.

The other information exchange occurs from the coarse scale to the fine scale. The boundary of an atomistic subdomain forms an artificial interface. Because an atom at the interface interacts with its neighboring atoms outside of the atomistic subdomain, we need to approximate the dynamics using the existing information. If no such approximation is made, there appear strong spurious wave reflections at the interface [31]. Extensive studies have been carried out to reduce such reflections. For instance, one may design special interfacial conditions using an artificial dissipation or a mixed Hamiltonian [4,19,30]. These methods do not have a clear error control, and may involve heuristic derivations and empirical parameters.

As an alternative, assuming that the waves are only generated within the atomistic subdomain due to strong nonlinearities or initial defects, one may reconstruct the fine dynamics of the neighboring atoms. The reconstruction can be made exact for a linear lattice through a time history treatment [2], which allows a fine scale wave to go across the interface transparently. This technique was developed for multiscale computations by Cai et al. [5], and further enhanced with displacement decomposition techniques in [12,13,28,31]. However, the time history treatment is accurate only for linear lattices. Because of the non-locality in time, it does not admit a nonlinear generalization. For a crystalline solid with small deformation, one ignores the nonlinear effects around the interface in the coarse scale, and adopts the interfacial condition corresponding to the lattice at equilibrium. This introduces error, and the reflection can be large for applications to nonlinear atomistic systems such as an anharmonic lattice [27,28]. In addition, it is numerically demanding to perform the convolutions. We notice that efforts have been made for local interfacial conditions in [15]. Along the line of [7], the authors minimize a thermal flux functional with a selected number of time steps and space stencil.

We further remark that for wave propagations in homogeneous media, there are various non-reflecting boundary conditions [8–11]. They do not apply to the atomistic systems, for which the propagation speed of a high frequency wave depends on its wave number via the discrete dispersion relationship.

Here we propose a new type of interfacial conditions, namely, velocity interfacial conditions. Briefly speaking, we regard that the fast fluctuations in the short length scale are carried by the long waves, and the long waves evolve in a slower time scale. Therefore, during each coarse scale time step, the fine scale waves around the interface are governed by a linearized system, with its parameters determined from the coarse grid solution. Making use of the uni-directional propagation of the fine scale fluctuations, we factorize the linearized system to obtain an expression for the velocity in terms of the displacement at several atoms within the atomistic subdomain. The dynamics of the interfacial atoms is then described by this velocity formulation, instead of the original acceleration formulation. We correct the velocity near the interface accordingly. In this way, we obtain a simple and effective interfacial condition. The linearization and velocity formulation are designed with required accuracies, and we may reach higher order of accuracy if more computing resources are available.

Because the condition is local in both space and time, it applies directly to crystalline solids with relatively strong nonlinearity and large deformation. Compared with [15], our interfacial condition only involves atomistic displacements at a single (current) time step, hence no time history memory or treatment is needed.

Designing a coarse grid scheme and an interfacial condition with balanced accuracy, we may obtain an efficient algorithm and reach required overall accuracy. Such a balance is important, as the errors at different scales contaminate with each other in multiscale simulations [27]. Through numerical examples in one and two space dimensions, we shall demonstrate that the finite difference approach yields an accuracy comparable to the pseudo-spectral multiscale method (PMM) in linear systems. For general lattices, PMM is accurate if and only if the nonlinearity is relatively weak [28]. In contrast, the proposed finite difference approach considerably enhances the resolution for strongly nonlinear systems, and takes a much reduced computing load.

The major features of the finite difference approach are as follows:

- We propose the first finite difference approach for multiscale simulations of crystalline solids with relatively strong nonlinearity and large deformation. Controllable high accuracy is reached in both scales.
- Adopting a wave view for the lattice dynamics, we propose velocity interfacial conditions that efficiently reduce reflections for nonlinear lattices.
- Solutions in both scales exist for a selected atomistic subdomain. Coarse grid finite difference schemes capture long waves accurately with low computing cost. Agreement between scales is forced through reassignment of the coarse grid value by fast averaging the fine scale solution.
- The algorithm is simple, clear, and with low computing load. It is easy for programing, and straightforward for applications in multiple dimensions.

The rest of this paper is organized as follows. We formulate the finite difference approach and velocity interfacial conditions in Section 2. We illustrate the approach through several examples, including a linear system of harmonic lattice, a nonlinear anharmonic lattice, a lattice with the Lennard-Jones potential in one space dimension, as well as a Slepyan fracture model in two space dimensions. A flow chart is presented in Section 3. We display the numerical results in Section 4, and make some concluding remarks in the last section. The matching differential operator method is sketched in an Appendix.

2. General formulation and interfacial conditions

Consider a crystalline solid in $\Omega \subset \mathbb{R}^3$, consisting of n_a atoms. The position of the nth atom at rest is x_n. Under suitable initial and boundary conditions, the motion of the system is governed by the Newton law:

$$M\ddot{u} = f + f_{\text{ext}} \tag{1}$$

with $u, f, f_{\text{ext}} \in \mathbb{R}^{3n_a}$ representing the displacement vector, internal force and external force, respectively. The mass matrix is $M = \text{diag}(m_1 I_{3\times 3}, \ldots, m_{n_a} I_{3\times 3})$, where $m_i > 0$. The internal force comes from interatomic interactions. It is described by a potential U depending on the displacement difference for all interacting atoms in the form of $|u_i - u_j|$. The internal force reads $f = -\nabla_u U$. Eq. (1) may be expressed componentwise as follows:

$$m_n \ddot{u}_n = -\frac{\partial U}{\partial u_n} + f_{\text{ext},n}. \tag{2}$$

We regard the complete atomistic Newton law (2) as an "exact" description to the lattice dynamics. The goal of a multiscale computation is a faithful resolution to the dynamics at a much reduced computing load.

A wave type of viewpoint is taken for the lattice dynamics. We regard that time evolution for the displacement at subsequent atoms forms a discrete wave profile. Short waves and long waves interact through the nonlinear terms in (2). For many applications, the influence of short waves is important only within a small subdomain Ω_A. Away from there, these short waves lay a negligible or homogenizable impact on the long wave evolution. Accordingly, fine scale computations are not performed away from the subdomain Ω_A. In particular, we denote $\Omega_B = \Omega \setminus \Omega_A$.

We cast a finite difference coarse grid in Ω. The grid points are denoted as $y_J \in \mathbb{R}^3$. A coarse grid displacement $d_J \in \mathbb{R}^3$ is assigned to represent the motion for atoms around y_J. To compute the coarse scale dynamics,

we adopt schemes designed by a matching differential operator method. To maintain the agreement with the fine scale dynamics, we reassign the coarse grid values by averaging the atomistic solution within Ω_A.

Meanwhile, an atom at the interface $\partial\Omega_A$ receives force from adjacent atoms in Ω_B. For such an interfacial atom, the force depends on the displacement at its adjacent atoms, which are not available in the multiscale computation. We therefore need to specify the dynamics at the interfacial atoms in a self-contained manner, that is, an interfacial condition is required. In this study, we allocate an interfacial layer $\Omega_L \subset \Omega_A$ with a width of several atoms. The velocity for atoms in Ω_L is computed from both the atomistic displacement in Ω_A and the information at the coarse grid points near the interface. The dynamics for Ω_L are governed in terms of the velocity for reflection reduction, in contrast to that for $\Omega_D \equiv \Omega_A \setminus \Omega_L$ governed by the Newton law in terms of the acceleration.

We describe the averaging procedure and the interfacial conditions in the following subsections.

2.1. Fast averaging technique

We describe an averaging technique for a one-dimensional lattice. Without loss of generality, we consider a lattice with the atoms equally distributed at rest. The coarse grid points are equally distributed as well, with a coarsening ratio p.

In the proposed finite difference approach, the coarse grid displacement d exists over the whole domain. Meanwhile, fine atomistic solution u_A exists in Ω_A. Because of the different meshes and schemes used, deviation appears and grows between these two solutions if no coupling is forced. It is conceivable that u_A represents better the dynamics in Ω_A. Hence we rectify d at each coarse time step to maintain the agreement between the two scales.

To this end, we first linearly interpolate d to obtain atomistic displacement in Ω. That is, we assign

$$\bar{u} = Nd. \tag{3}$$

Here N is the linear shape function matrix

$$N = \begin{bmatrix} 1 & & & & \\ a & b & & & \\ & \ddots & \ddots & & \\ & & & a & b \end{bmatrix} \tag{4}$$

with $a = \frac{1}{p}[p-1,\ldots,1,0]^{\mathrm{T}}$, and $b = \frac{1}{p}[1,\ldots,p]^{\mathrm{T}}$.

Next, we rectify displacement in Ω_A. More precisely, for N_A and N_B the interpolation submatrices corresponding to Ω_A and Ω_B, respectively, we take the linear interpolation in Ω_B and the atomistic solution in Ω_A to form

$$u \approx \begin{bmatrix} u_A \\ N_B d \end{bmatrix}. \tag{5}$$

For this u, we compute a new coarse grid displacement $\tilde{d}$. To obtain an optimal coarse grid representation, we define a global error function $(u - N\tilde{d})^{\mathrm{T}}(u - N\tilde{d})$. Minimization for the error leads to

$$\tilde{d} = M_{\mathrm{e}}^{-1} N^{\mathrm{T}} u = M_{\mathrm{e}}^{-1} N^{\mathrm{T}} \begin{bmatrix} u_A \\ N_B d \end{bmatrix} \tag{6}$$

with a matrix $M_{\mathrm{e}} = N^{\mathrm{T}}N$.

This expression uses the inversion for M_{e}, and $M_{\mathrm{e}}^{-1}N^{\mathrm{T}}$ is typically a full matrix. In practice, we observe that most entries in each row are very close to zero. Moreover, the non-negligible entries in a row are almost the same as in other rows, except for a shift. For example, we take $p = 10$ and $n_a = 801$. The 20th and 40th rows in $M_{\mathrm{e}}^{-1}N^{\mathrm{T}}$ are displayed in Fig. 1a. The difference between these two rows, up to a shift, may be found as small as 10^{-18}. Moreover, for a much smaller atomistic system with 201 atoms, the non-negligible entries are again the same, with an error on the order of 10^{-8}. See Fig. 1(b).

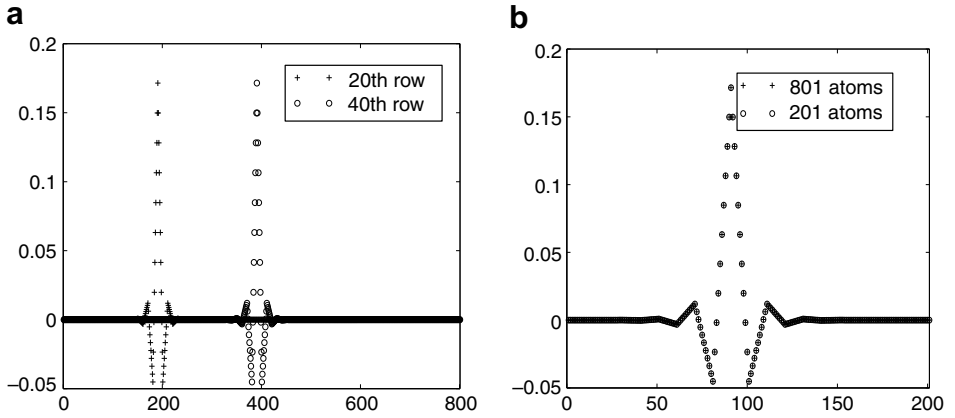

Fig. 1. Averaging technique: (a) two rows in $M_e^{-1}N^T$; (b) the 10th row in $M_e^{-1}N^T$ for two atomistic systems of different size.

The observation suggests us compute $M_e^{-1}N^T$ for a much smaller atomistic system. Taking a selected subrow for non-negligible entries, we use these entries to average the full atomistic system.

We make a few remarks for implementation of the fast averaging technique.

First, in all the numerical examples presented later, we take $(8p+1)$ non-negligible entries for averaging. This means, for a coarse grid point y_J, we take d_J as a weighted average of the atomistic displacements at the $(8p+1)$ atoms around it.

Secondly, for a coarse grid point near the interface, we are lack of adequate fine scale information from the side of Ω_B. There are different ways to treat this problem. We may develop an approximate averaging technique that uses only the information from Ω_A. As a matter of fact, the first and last several rows in $M_e^{-1}N^T$ are not uniform. The non-negligible entries provide weights for an unbalanced average. Again we compute these entries for a selected small system, and perform unbalanced fast average to obtain the coarse scale displacement at a coarse grid point near the interface. Simulations in two space dimensions presented later are carried out in this manner. Alternatively, one may simply ignore the reassignment at several such coarse grid points.

Finally, we remark that the fast averaging technique directly applies to the reassignment for the coarse grid velocity $\dot{d}$. In two space dimensions, we simply perform the average in one dimension first, and then the other dimension. A more involved averaging algorithm may also be designed in a similar way by using two-dimensional linear shape functions.

To summarize, we approximate the submatrix of $M_e^{-1}N^T$ that corresponds to Ω_A by a sparse matrix C_A. We keep the coarse grid values in Ω_B unchanged, and reassign those in Ω_A by a weighted average, where the weights are computed from $M_e^{-1}N^T$ for a selected small system. Formally, we have

$$\tilde{d} = \begin{bmatrix} C_A u_A \\ d_B \end{bmatrix}. \tag{7}$$

2.2. Velocity interfacial conditions

Reflection reduction is crucial for multiscale computations. While a coarse grid scheme matters mainly the quality of the numerical resolution, the reflections directly enter the atomistic subdomain where the physics is important and nonlinearity may be strong. In the presence of reflection, the solution usually becomes incorrect.

To reduce the reflection, certain artificial dissipative mechanisms such as damping may be introduced [30]. One may also use a mixed Lagrangian or potential for the two scales [1]. The reflections are then smeared out or smoothed. These methods usually involve heuristic arguments and empirical parameters, and the accuracy is not controllable in general. Furthermore, there seems no direct way to perform mathematical analysis on these methods.

Another class of methods intend to solve exactly the linear lattice. Assuming that all waves are generated from the atomistic subdomain, one records the displacement history at the interfacial atoms. Applying the Laplace transform to the linear lattice, displacements at all atoms in Ω_B may be reconstructed from the time history information [2,5]. By splitting the displacement into its long wave part (mean displacement) and short wave part (fine fluctuation), one applies the time history treatment to the fine fluctuation only, and obtains a better resolution [27,28,31]. In particular, together with a normal mode decomposition and a coarse grid scheme derived by the matching differential operator method, the pseudo-spectral multiscale method (PMM) reaches high accuracy for linear lattices. However, there are several major difficulties in applying this type of methods with the time history treatment. First, the reconstruction involves a convolution, which is numerically demanding. Secondly, it may take great efforts to compute the kernel functions for convolution in multiple-dimensional applications [21,23]. Moreover, the vital drawback appears when the time history treatment is applied to a nonlinear system. Due to the nonlinearity, waves with different length scales interact with each other. The long wave amplitude may change considerably across the interface as time evolves. Because the time history treatment is based on linear approximation for the whole cut-off time period, there is no direct way to generalize this treatment to nonlinear situations. If one blindly adopts the time history treatment to a nonlinear lattice, reflections appear even all other parts of the algorithm are accurate [28]. We shall describe this difficulty for the bridging scale method (BSM), and PMM through numerical tests with the anharmonic lattice.

In the following, we propose a velocity interfacial condition. We start with the harmonic lattice. The general formulation for nonlinear systems are then illustrated. We also show how to handle multiple dimensions.

2.2.1. A motivating example: velocity interfacial conditions for the harmonic lattice

Consider a harmonic lattice in Fig. 2. The atomistic subdomain Ω_A contains the atoms numbered 1 through n_b. The Newton equation for the nth atom reads

$$\ddot{u}_n = u_{n-1} - 2u_n + u_{n+1}. \tag{8}$$

Imagining $z(x,t)$ as a continuous displacement such that $u_n(t) = z(x_n,t)$, we perform the Taylor expansion around u_n to obtain

$$\left[\frac{\partial^2}{\partial t^2} - \sum_{m=1}^{\infty} \frac{2}{(2m)!}\frac{\partial^{2m}}{\partial x^{2m}} h_a^{2m}\right] z = 0. \tag{9}$$

Here h_a is the atomistic spacing at equilibrium. The differential operator is factorized as follows:

$$\left[\frac{\partial}{\partial t} + \sum_{i=1}^{\infty} a_i h_a^i \frac{\partial^i}{\partial x^i}\right]\left[\frac{\partial}{\partial t} + \sum_{i=1}^{\infty} b_i h_a^i \frac{\partial^i}{\partial x^i}\right] z = 0, \tag{10}$$

where a_i and b_i are coefficients to be determined.

Regarding h_a as a small quantity, we take $a_1 = -1, b_1 = 1$ on the leading order. We speculate that the two factors of the differential operator correspond to the left-going and the right-going waves, respectively. Under the assumption that waves propagate into Ω_B, where fine fluctuations do not present initially, we find that

$$\left[\frac{\partial}{\partial t} + \sum_{i=1}^{\infty} b_i h_a^i \frac{\partial^i}{\partial x^i}\right] z = C_0 \tag{11}$$

with C_0 a constant. This implies that for $j \geqslant 1$

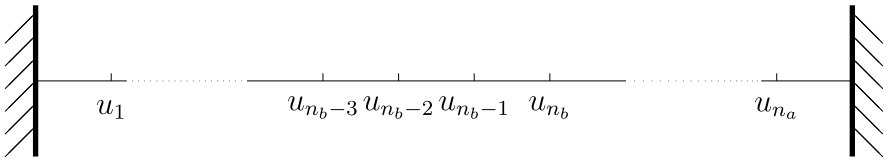

Fig. 2. Harmonic lattice in one space dimension.

$$\frac{\partial}{\partial t}\frac{\partial^j}{\partial x^j}z = -\sum_{i=1}^{\infty} b_i h_a^{i+j}\frac{\partial^{i+j}}{\partial x^{i+j}}z. \tag{12}$$

Substituting this into (10), we deduce after some manipulations that $a_i = -b_i$, and

$$\sum_{m=1}^{\infty}\frac{2}{(2m)!}\frac{\partial^{2m}}{\partial x^{2m}}h_a^{2m}z = \left[\sum_{i=1}^{\infty} b_i h_a^i\frac{\partial^i}{\partial x^i}\right]^2 z. \tag{13}$$

By equating terms on the same order of h_a, we obtain for $n \in \mathbb{N}$ that

$$\sum_{i=1}^{n} b_i b_{2n+1-i} = 0, \quad \sum_{i=1}^{n-1} 2b_i b_{2n-i} + b_n^2 = \frac{2}{(2n)!}. \tag{14}$$

Then the coefficients are computed recursively.

Retaining different number of terms, we obtain a class of interfacial conditions with different order of accuracy.

Second order: Direct calculation shows that $b_2 = 0$. Eq. (11) reads

$$\left(\frac{\partial}{\partial t} + h_a\frac{\partial}{\partial x} + \mathrm{o}(h_a^2)\right)z = C_0. \tag{15}$$

Neglecting the residual $\mathrm{o}(h_a^2)$, one obtains precisely the characteristic equation for the linear wave propagation. If there is no wave initially in Ω_B, we have $C_0 = 0$ and

$$\left(\frac{\partial}{\partial t} + h_a\frac{\partial}{\partial x}\right)z = \mathrm{o}(h_a^2). \tag{16}$$

It suggests an interfacial condition in the continuous form as follows:

$$\dot{z} = -h_a\frac{\partial}{\partial x}z + \mathrm{o}(h_a^2). \tag{17}$$

Applying this at the n_bth atom, we obtain an expression for the velocity by taking an upwind discretization of z_x:

$$\dot{u}_{n_b} = u_{n_b-1} - u_{n_b}. \tag{18}$$

This is a first-order velocity interfacial condition, because the truncation error is on the order of $\mathrm{o}(h_a^2)$ in the upwind approximation. We remark that this corresponds to the continuous non-reflecting boundary condition in the pioneering work by Engquist and Majda [8].

The interfacial condition (18) dissipates waves from Ω_A. To see this, we define a total energy

$$E(t) = \frac{1}{2}\sum_{n=1}^{n_b-1}\dot{u}_n^2 + \frac{1}{2}\sum_{n=1}^{n_b-1}(u_{n+1}-u_n)^2. \tag{19}$$

If we impose a fixed end $u_1 = 0$, then we derive from the Newton law (8) that

$$\begin{aligned}\frac{\mathrm{d}E}{\mathrm{d}t} &= \sum_{n=1}^{n_b-1}\dot{u}_n\ddot{u}_n + \sum_{n=1}^{n_b-1}(u_{n+1}-u_n)(\dot{u}_{n+1}-\dot{u}_n)\\ &= \dot{u}_{n_b}(u_{n_b}-u_{n_b-1})\\ &= -(u_{n_b}-u_{n_b-1})^2.\end{aligned} \tag{20}$$

The energy decreases as long as $u_{n_b} - u_{n_b-1} \neq 0$.

We make a few remarks.

First, though condition (18) is dissipative, it is not an optimal condition. When this condition is applied, reflection occurs and propagates back to Ω_A, leaving $u_{n_b} - u_{n_b-1} \sim 0$.

Secondly, condition (18) assigns the velocity rather than the displacement for the interfacial atom. To obtain the displacement u_{n_b}, we integrate it numerically.

Thirdly, the accuracy may be readily enhanced to $o(h_a^2)$. Let $\Delta_1 = u_{n_b} - u_{n_b-1}, \Delta_2 = u_{n_b} - u_{n_b-2}$. We solve from the Taylor expansions

$$\begin{bmatrix} \Delta_1 \\ \Delta_2 \end{bmatrix} = \begin{bmatrix} 1 & 1 \\ 2 & 4 \end{bmatrix} \begin{bmatrix} h_a z_x \\ \frac{h_a^2}{2} z_{xx} \end{bmatrix} + o(h_a^2), \tag{21}$$

that

$$\begin{bmatrix} h_a z_x \\ \frac{h_a^2}{2} z_{xx} \end{bmatrix} = \begin{bmatrix} 2 & -1/2 \\ -1 & 1/2 \end{bmatrix} \begin{bmatrix} \Delta_1 \\ \Delta_2 \end{bmatrix} + o(h_a^2). \tag{22}$$

Combining (17) and (22), we design a second-order velocity interfacial condition

$$\dot{u}_{n_b} = \frac{1}{2}(-u_{n_b-2} + 4u_{n_b-1} - 3u_{n_b}). \tag{23}$$

This condition has a smaller truncation error, and involves one more atom compared with (18).

Finally, with the displacements u_{n_b-2}, u_{n_b-1} and u_{n_b}, we may also rectify the velocity at the next atom to the same order of accuracy:

$$\dot{u}_{n_b-1} = \frac{1}{2}(u_{n_b-2} - u_{n_b}). \tag{24}$$

Noticing that u_{n_b-2}, u_{n_b-1} and u_{n_b} locate at the downwind side for the (n_b-2)th atom, we do not correct $\dot{u}_{n_b-2}$ with these three displacements.

Higher orders: From (14), we compute that $b_{2n} = 0$ and $b_1 = 1, b_3 = 1/24, b_5 = 1/192$. The fourth-order condition reads

$$\dot{z} = -h_a \frac{\partial}{\partial x} z - \frac{h_a^3}{24} \frac{\partial^3}{\partial x^3} z + o(h_a^4). \tag{25}$$

To design a discrete interfacial condition, we consider the Taylor expansions of $\Delta_i = u_{n_b-i} - u_{n_b}$ for $i = 1, 2, 3, 4$:

$$\begin{bmatrix} \Delta_1 \\ \Delta_2 \\ \Delta_3 \\ \Delta_4 \end{bmatrix} = \begin{bmatrix} -1 & 1 & -1 & 1 \\ -2 & 4 & -8 & 16 \\ -3 & 9 & -27 & 81 \\ -4 & 16 & -64 & 256 \end{bmatrix} \begin{bmatrix} h_a z_x \\ \frac{h_a^2}{2} z_{xx} \\ \frac{h_a^3}{6} z_{xxx} \\ \frac{h_a^4}{24} z_{xxxx} \end{bmatrix} + o(h_a^4). \tag{26}$$

It is solved by

$$\begin{bmatrix} h_a z_x \\ \frac{h_a^2}{2} z_{xx} \\ \frac{h_a^3}{6} z_{xxx} \\ \frac{h_a^4}{24} z_{xxxx} \end{bmatrix} = \begin{bmatrix} -4 & 3 & -4/3 & 1/4 \\ -13/3 & 17/4 & -7/3 & 11/24 \\ -3/2 & 2 & -7/6 & 1/4 \\ -1/6 & 1/4 & -1/6 & 1/24 \end{bmatrix} \begin{bmatrix} \Delta_1 \\ \Delta_2 \\ \Delta_3 \\ \Delta_4 \end{bmatrix} + o(h_a^4). \tag{27}$$

Together with (25), this leads to a fourth-order condition:

$$\dot{u}_{n_b} = -\frac{5}{16}u_{n_b-4} + \frac{13}{8}u_{n_b-3} - \frac{7}{2}u_{n_b-2} + \frac{35}{8}u_{n_b-1} - \frac{35}{16}u_{n_b}. \tag{28}$$

In the same way, we rectify velocities at the next two atoms as follows:

$$\dot{u}_{n_b-1} = \frac{1}{16}u_{n_b-4} - \frac{3}{8}u_{n_b-3} + \frac{5}{4}u_{n_b-2} - \frac{5}{8}u_{n_b-1} - \frac{5}{16}u_{n_b}, \tag{29}$$

$$\dot{u}_{n_b-2} = -\frac{1}{16}u_{n_b-4} + \frac{5}{8}u_{n_b-3} - \frac{5}{8}u_{n_b-1} + \frac{1}{16}u_{n_b}. \tag{30}$$

Velocities at atoms further inside Ω_A are not corrected, due to considerations on the wave propagation direction.

2.2.2. Interfacial conditions for nonlinear lattices

Nonlinearity exists in most applications. For a nonlinear system, an exact interfacial condition requires precise expression for the solution, which is not accessible in general. Because other existing interfacial treatments are less accurate even for the linear lattices, we discuss here only the time history treatment. If the nonlinearity is weak, one may adopt an interfacial condition corresponding to the linear lattice at equilibrium [5,28,31]. This introduces an error. When the nonlinearity is strong, the error can be large. Because a long time history is necessary for performing convolutions, one can not update the time history kernel within the cut-off period. Moreover, the kernel function is hard to compute when the lattice is away from the uniform equilibrium.

In contrast, the velocity interfacial conditions developed in the last subsection are local in both space and time. At any fixed time, an atom near the interface experiences the lattice approximately as a linear one with a uniform strain, which is determined by the coarse scale displacement at these several grid points around the interface. This suggests a treatment using a linearized lattice

$$\ddot{u}_n = c^2(t)(u_{n-1} - 2u_n + u_{n+1}), \tag{31}$$

where $c(t)$ is computed through d_J's near the interface. There are various ways to compute $c(t)$. For instance, we may decompose the acceleration term in the Newton law into the multiplication of a factor $u_{n-1} - 2u_n + u_{n+1}$, and another factor approximated by the d_J's. Alternatively, we may perform the Taylor expansion to find the coefficient for u_{xx}, and approximate the coefficient in terms of d_J's.

When the lattice is at equilibrium in Ω_B initially, the velocity interfacial condition for the nonlinear lattice is taken as follows:

$$\begin{bmatrix} \dot{u}_{n_b-2} \\ \dot{u}_{n_b-1} \\ \dot{u}_{n_b} \end{bmatrix} = c(t) \begin{bmatrix} -1/16 & 5/8 & 0 & -5/8 & 1/16 \\ 1/16 & -3/8 & 5/4 & -5/8 & -5/16 \\ -5/16 & 13/8 & -7/2 & 35/8 & -35/16 \end{bmatrix} \begin{bmatrix} u_{n_b-4} \\ u_{n_b-3} \\ u_{n_b-2} \\ u_{n_b-1} \\ u_{n_b} \end{bmatrix}. \tag{32}$$

An anharmonic lattice: With a parameter $\overline{K}$ characterizing the nonlinearity, the Newton law for nth atom is

$$\ddot{u}_n = u_{n-1} - 2u_n + u_{n+1} + \frac{\overline{K}}{h_a^2}\left[(u_{n+1} - u_n)^3 - (u_n - u_{n-1})^3\right]. \tag{33}$$

We notice that

$$(u_{n+1} - u_n)^3 - (u_n - u_{n-1})^3 = (u_{n+1} - 2u_n + u_{n-1})[(u_{n+1} - u_n)^2 + (u_{n+1} - u_n)(u_n - u_{n-1}) + (u_n - u_{n-1})^2]. \tag{34}$$

For the anharmonic lattice (33), we take

$$c_{\mathrm{AH}}^2(t) = 1 + \frac{3\overline{K}(d_{J+1} - d_J)^2}{p^2 h_a^2}. \tag{35}$$

The lattice with the Lennard-Jones potential: The governing equation for the displacement u_n is

$$\ddot{u}_n = -48[(r_0 + u_{n+1} - u_n)^{-13} - (r_0 + u_n - u_{n-1})^{-13}] + 24[(r_0 + u_{n+1} - u_n)^{-7} - (r_0 + u_n - u_{n-1})^{-7}]. \tag{36}$$

Here $r_0 = 2^{1/6}$ is the atomic distance at rest. After some manipulations, we find

$$-(r_0 + u_{n+1} - u_n)^{-k} + (r_0 + u_n - u_{n-1})^{-k} = (u_{n+1} - 2u_n + u_{n-1}) \sum_{l=0}^{k-1} (r_0 + u_{n+1} - u_n)^{-k+l} (r_0 + u_n - u_{n-1})^{-1-l}. \tag{37}$$

We approximate $c^2(t)$ by

$$c_{\mathrm{LJ}}^2(t) = 624[r_0 - (d_{J+1} - d_J)/p]^{-14} - 168[r_0 - (d_{J+1} - d_J)/p]^{-8}. \tag{38}$$

2.2.3. A multi-dimensional example – the Slepyan model for fracture

A Slepyan model describes dynamic Mode III fracture in a square lattice [25]. With a damping coefficient $b \geqslant 0$, the displacement out of the lattice plane u_{ij} is governed by

$$\ddot{u}_{ij} = -b\dot{u}_{ij} + \sum_{i',j'}(u_{i'j'} - u_{ij})\Theta(2 - |u_{i'j'} - u_{ij}|). \tag{39}$$

Here Θ denotes the Heaviside step function. Away from the fracture, the lattice is harmonic in both dimensions. One may allocate an atomistic subdomain Ω_A so that the fluctuations (short waves) propagate along the normal direction of the interface. A one-dimensional interfacial condition then applies across the interface.

However, for more general situations, we need to determine the wave propagation direction. To this end, let us consider a continuous linear wave equation

$$u_{tt} = h_a^2(u_{xx} + u_{yy}). \tag{40}$$

For a plane wave $u(x, y, t) = u(x\cos\alpha + y\sin\alpha - ct)$ with an incline angle α, we compute

$$u_{tx} = -cu''\cos\alpha, \quad u_{ty} = -cu''\sin\alpha. \tag{41}$$

We determine the angle α from the velocity gradient by

$$\tan\alpha = \frac{u_{ty}}{u_{tx}}. \tag{42}$$

We rotate the axes to (ξ, η) coordinates by the angle α. The Laplacian remains in the same form, and Eq. (40) becomes

$$u_{tt} = h_a^2(u_{\xi\xi} + u_{\eta\eta}). \tag{43}$$

Because the wave propagates along ξ-direction, it solves a one-dimensional equation

$$u_{tt} = h_a^2 u_{\xi\xi}. \tag{44}$$

A first-order velocity interfacial condition is derived in continuous form:

$$\dot{u} + h_a\frac{\partial}{\partial\xi}u = C. \tag{45}$$

Back to the original coordinates, we take

$$\dot{u} + h_a(u_x\cos\alpha + u_y\sin\alpha) = C. \tag{46}$$

This motivates velocity interfacial conditions in a multiscale computation as follows.

First, as previously mentioned, the fine scale oscillations are carried by the long waves in the coarse scale. Therefore, we compute the angle from the coarse grid velocity, e.g.

$$\tan\alpha = \frac{\dot{d}_{I,J+1} - \dot{d}_{I,J-1}}{\dot{d}_{I+1,J} - \dot{d}_{I-1,J}}. \tag{47}$$

Secondly, we design velocity interfacial conditions along each dimension with required order of accuracy.

Finally, we superpose the conditions with the coefficients $\cos\alpha$ and $\sin\alpha$.

More precisely, let the interface lies horizontally at the jth layer in the fine scale, and between the Jth layer and the $(J+1)$th layer in the coarse grid. For each i, a fourth-order velocity interfacial condition reads

$$\begin{bmatrix} \dot{u}_{i,j-2} \\ \dot{u}_{i,j-1} \\ \dot{u}_{i,j} \end{bmatrix} = \cos\alpha \begin{bmatrix} u_{i-2,j-2} & u_{i-1,j-2} & u_{i+1,j-2} & u_{i+2,j-2} \\ u_{i-2,j-1} & u_{i-1,j-1} & u_{i+1,j-1} & u_{i+2,j-1} \\ u_{i-2,j} & u_{i-1,j} & u_{i+1,j} & u_{i+2,j} \end{bmatrix} \begin{bmatrix} -1/16 \\ 5/8 \\ -5/8 \\ 1/16 \end{bmatrix}$$

$$+\sin\alpha\begin{bmatrix}-1/16 & 5/8 & 0 & -5/8 & 1/16\\ 1/16 & -3/8 & 5/4 & -5/8 & -5/16\\ -5/16 & 13/8 & -7/2 & 35/8 & -35/16\end{bmatrix}\begin{bmatrix}u_{i,j-4}\\ u_{i,j-3}\\ u_{i,j-2}\\ u_{i,j-1}\\ u_{i,j}\end{bmatrix}. \tag{48}$$

We remark that if the displacement is non-zero initially, a certain constant may be computed and added to the right-hand side.

2.2.4. Summary

Depending on the number of atoms that we rectify the velocities, we allocate an interfacial layer $\Omega_L \subset \Omega_A$. Let the dynamics for atoms in Ω_L being described by $(u_L, \dot{u}_L)$, and that for atoms in $\Omega_D = \Omega_A \setminus \Omega_L$ by $(u_D, \dot{u}_D)$. We formulate a matrix C_I and a velocity interfacial condition in terms of

$$\dot{u}_L = C_I u_A. \tag{49}$$

3. Numerical implementation

3.1. Time integration

For time integration of both the atomistic computations of u_D and the coarse grid computations of d, we adopt a verlet algorithm. We illustrate this algorithm for $\ddot{q} = F(q,t)$.

For a time step size Δt and data $q(t^l) = q^l, \dot{q}(t^l) = \dot{q}^l$, we compute

$$q^{l+1} = q^l + \dot{q}^l \Delta t + F(q^l, t^l)\frac{(\Delta t)^2}{2}, \tag{50}$$

$$\dot{q}^{l+1} = \dot{q}^l + \frac{\Delta t}{2}(F(q^l, t^l) + F(q^{l+1}, t^{l+1})). \tag{51}$$

For the multiscale computations, we use a mixed time integration technique. That is, we take a time step size $\Delta\tau$ for computing u_A, and $\Delta t = m\Delta\tau$ for computing d ($m \in \mathbb{N}$).

Furthermore, in the interfacial layer Ω_L, we simulate the dynamics by

$$u_n^{l+1} = u_n^l + \frac{\Delta\tau}{2}(\dot{u}_n^l + \dot{u}_n^{l+1}), \tag{52}$$

where the velocities $\dot{u}_n^l$ and $\dot{u}_n^{l+1}$ are obtained through the velocity interfacial conditions (49).

3.2. A flow chart

We summarize the finite difference approach in the following list. Please refer to Fig. 3 for illustration:

1. Atomistic computation in Ω_A
   - With the coarse grid displacement d and velocity $\dot{d}$ around the interface at current coarse time step t^l, compute the wave propagation coefficient $c(t)$, and the direction in case of multiple dimensions. Form the matrix C_I to be used in the velocity interfacial conditions (49).
   - At each sub-time step $t^l + j\Delta\tau$ ($j = 1, \ldots, m$), we compute the fine scale dynamics from a subsystem of (1) and the velocity interfacial conditions:

$$M_D\ddot{u}_D = f_D + f_{\text{ext},D}, \tag{53}$$

$$\dot{u}_L = C_I u_A. \tag{54}$$

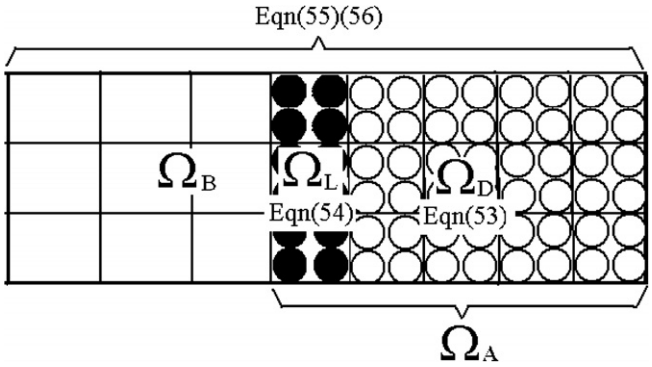

Fig. 3. Illustration of the computing mesh.

2. Coarse grid computation
   - We compute $(d^{l+1}, \dot{d}^{l+1})$ with the scheme designed by the matching differential operator method (62)

$$\ddot{d} = A(d). \tag{55}$$

   - Making use of the fine scale solution at $t^{l+1} = t^l + m\Delta\tau$, we reassign the coarse grid displacement and velocity by (7)

$$\begin{bmatrix} C_A u_A^{l+1} \\ d_B^{l+1} \end{bmatrix} \to d^{l+1}, \quad \begin{bmatrix} C_A \dot{u}_A^{l+1} \\ \dot{d}_B^{l+1} \end{bmatrix} \to \dot{d}^{l+1}. \tag{56}$$

3.3. Computational costs

The computational costs for each time step Δt mainly consist of four parts. First, the time integration for atoms in Ω_A causes a computing load on the order of $O(mn_A)$, with n_A the number of atoms in this subdomain. Secondly, the interfacial conditions result in a computing load on the order of $o(mn_A)$. Thirdly, the time integration for coarse grid values requires $O(n_C)$ computations for the n_C coarse grid points. Finally, the reassignment for the coarse grid values within Ω_A results in $O(n_A)$ computations. Summing them together, we obtain the total computing cost at a time step Δt as $O(mn_A + n_C)$. As a matter of fact, the computational cost is at least on this order for a concurrent multiscale simulation.

In contrast, an atomistic simulation for the entire system yields a computing load on the order of $O(mn_a)$. The total atom number n_a is typically much larger than n_A and n_C.

To make further comparisons, we remark that PMM and the bridging scale method yield computational costs on the order of $O(n_C \log n_C + m * (n_G(n_H + \log n_G) + n_A))$ and $O(n_C + m * (n_G n_H + n_A))$, respectively [28]. Here n_G denotes the number of ghost point atoms, and $n_H\tau$ is the length for the cut-off time, which should be chosen big enough to maintain the accuracy.

On the other hand, most finite element approaches result in algebraic systems, requiring additional computations and memory.

In summary, the proposed finite difference approach requires a much reduced computing load, compared with either the full atomistic computation, or other concurrent multiscale methods. We shall demonstrate in the next section that it reaches an accuracy comparable to PMM in case of linear systems. It considerably enhances the performance for nonlinear systems.

4. Numerical results

To demonstrate the nice features of the proposed finite difference approach, we present some numerical results for the harmonic lattice, the anharmonic lattice, the lattice with the Lennard-Jones potential, as well as the Slepyan model for fracture. We make comparisons with computations by full atomistic simulations,

the accurate yet more expensive pseudo-spectral multiscale method (PMM), the less accurate bridging scale method (BSM) [27] and the perfectly matched multiscale simulations (PMMS) [30]. In the following, we shall refer to the exact solution u as the one obtained from the full atomistic simulation. Meanwhile, for the multiscale computations, we use u_A to denote a solution by the atomistic computation in Ω_A, and d to represent that by coarse grid computation in Ω.

Real applications typically have a much larger degree of freedom than the numerical examples reported in this paper. Therefore, the advantages in accuracy and numerical efficiency would be much more significant when one adopts multiscale methods, and particularly the proposed finite difference approach.

4.1. Harmonic lattice

We use the harmonic lattice to test the multiscale methods.

In the numerical simulations, we take $h_a = 0.005$ and $p = 10$. The initial condition is given by $u_n(0) = u^0(x_n)$ with

$$u^0(x) = \begin{cases} 0.005\frac{e^{-100x^2}-e^{-6.25}}{1-e^{-6.25}}(1+0.1\cos(80\pi x)), & \text{for } |x| \leqslant 0.25; \\ 0, & \text{elsewhere.} \end{cases} \tag{57}$$

The computations are performed with a fine grid time step size $\Delta\tau = 0.005$ for $(x,t) \in [-2,2] \times [0,150]$. In all the multiscale computations, we take an atomistic subdomain $\Omega_A = [-0.375, 0.375]$, and a coarse grid time step size $\Delta t = 0.05$.

It is known that a wave propagates at a finite speed, and the lattice is essentially at equilibrium away from such waves. Further noticing the symmetry $x \to -x$ in the system, we plot solutions only in part of the computing domain.

First, we depict the numerical results by the finite difference approach with the MDO-4 scheme for the coarse grid and the fourth-order velocity interfacial condition. In Fig. 4, we display four snapshots for the solution at $t = 50$, 100, 130 and 150. The initial data contain mainly a long smooth wave and a short oscillatory wave. Both waves locate inside the atomistic subdomain Ω_A initially. Because of the dispersion, the oscillatory part moves slower. At $t = 50$, the long wave starts to go across the interface between Ω_A and Ω_B. In the next subplot for $t = 100$, the long wave mainly lies in Ω_B, and the short wave is going across the interface.

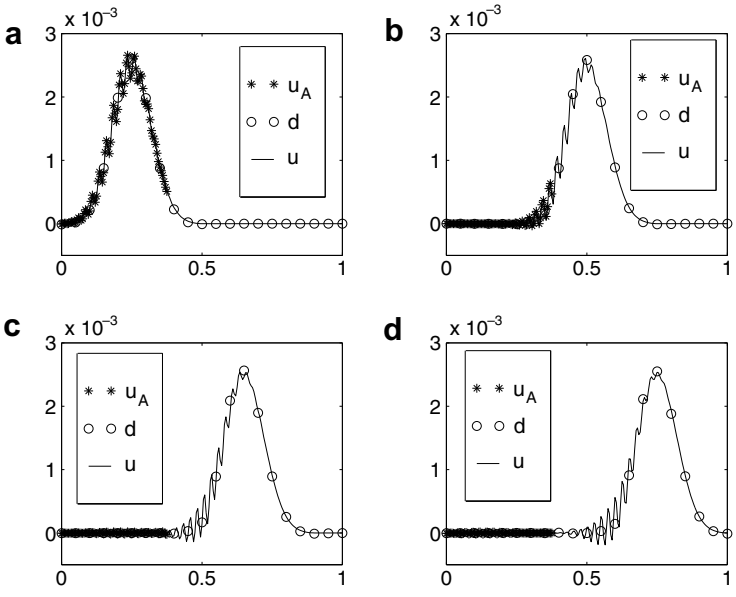

Fig. 4. Harmonic lattice by the finite difference approach: (a) $u(x,50)$; (b) $u(x,100)$; (c) $u(x,130)$; (d) $u(x,150)$.

Later at $t = 130$ and $t = 150$, the short wave leaves Ω_A. From the figure, we observe that the exact solution u is faithfully reproduced in both Ω_A and Ω_B by the finite difference approach. The numerical reflection in Ω_A at $t = 130$ or 150 is very small.

In contrast, if we take the second-order velocity interfacial condition instead, the reflection in Ω_A increases. See Fig. 5. The reflection is negligible in the early stages, e.g. in subplots (a) and (b). An observable reflected wave is shown in subplot (c), after the short wave goes across the interface. It propagates back toward Ω_A, as seen in subplot (d).

The resolution by PMM (pseudo-spectral multiscale method) in Fig. 6 is comparable to that by the finite difference approach with the fourth-order velocity interfacial condition. We notice that PMM is numerically more expensive, particularly due to the convolution for treating the interfaces.

BSM (bridging scale method) produces larger reflections in Ω_A and observable deviation in the coarse grid points over Ω_B, as shown in Fig. 7. It is known that even with a more accurate coarse grid scheme, the reflections are not reduced. The reflection is mainly due to an inaccuracy in the interfacial condition with the linear displacement decomposition. More detailed analysis on numerical costs and error study may be found in [27].

PMMS (perfectly matched multiscale simulations) gives a resolution slightly better than BSM [30]. Yet it is crucial for such a good resolution to carefully tune the artificial parameters. The reflection may be much larger if the parameters are not chosen properly, or the PML (perfectly matched layer) width is not big enough. In this simulation 20 atoms are taken near each interface. In contrast, the finite difference approach only assigns an interfacial layer of 3 atoms for the fourth-order velocity interfacial condition. Furthermore, because a linear element is used for the coarse scale computations, the propagating speed of the long wave exceeds that for the exact solution. See Fig. 8. We remark that the coarse grid resolution may be enhanced by coupling the PML idea with the coarse grid schemes derived by the matching differential operator method [32].

We illustrate the detailed numerical reflections for the aforementioned multiscale methods in Fig. 9. We observe that the fourth-order velocity interfacial condition produces a reflection on the same order of magnitude as PMM, while the second-order velocity interfacial condition is comparable to BSM. The result by PMMS gives a reflection with an amplitude in between. We also observe that the reflections by the proposed finite difference approach are in the form of a wave package containing both short and long waves. The results by PMM and BSM, in contrast, mainly contain the long wave components.

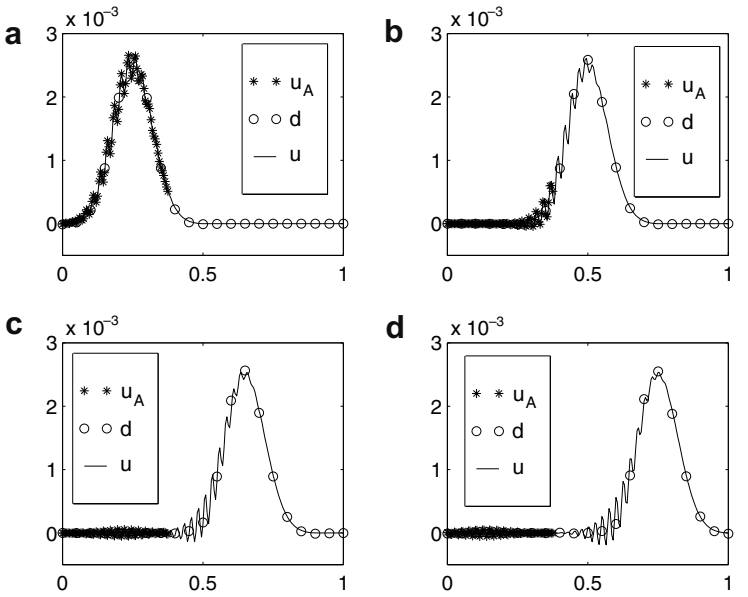

Fig. 5. Harmonic lattice by the finite difference approach with the second-order velocity interfacial condition: (a) $u(x, 50)$; (b) $u(x, 100)$; (c) $u(x, 130)$; (d) $u(x, 150)$.

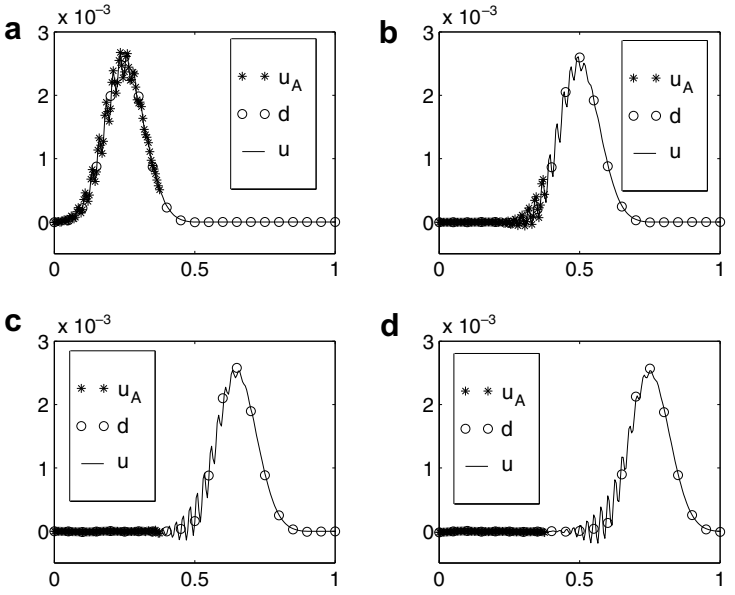

Fig. 6. Harmonic lattice by PMM: (a) $u(x, 50)$; (b) $u(x, 100)$; (c) $u(x, 130)$; (d) $u(x, 150)$.

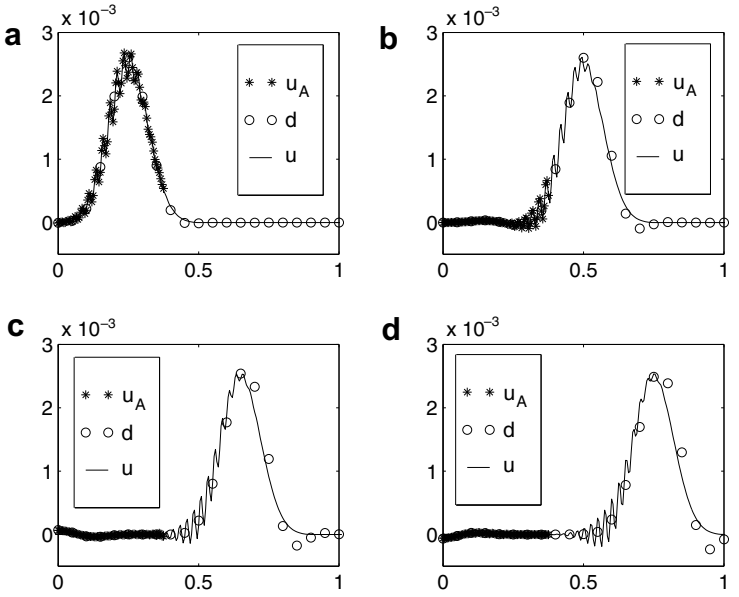

Fig. 7. Harmonic lattice by bridging scale method: (a) $u(x, 50)$; (b) $u(x, 100)$; (c) $u(x, 130)$; (d) $u(x, 150)$.

4.2. Nonlinear lattices in one space dimension

4.2.1. Anharmonic lattice

In the following, we make comparisons for the finite difference approach, BSM and PMM. The parameter $\overline{K}$ represents the strength of nonlinearity. In this study, we show the results for $\overline{K} = 30$ and $\overline{K} = 50$. The initial data (57) contain a wave on the order of $h_a = 0.005$, and these two cases correspond to fairly strong nonlinearity. In a previous study of the same problem by PMM, the nonlinearity parameter was chosen as $\overline{K} = 10$ [28].

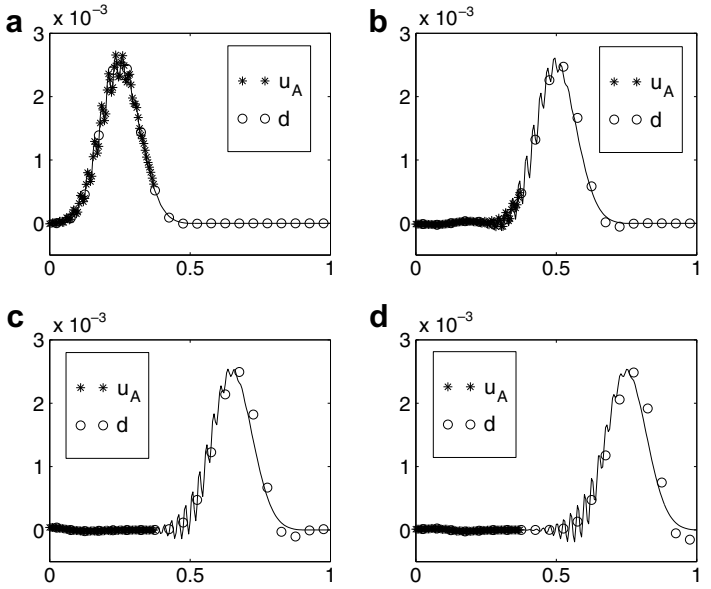

Fig. 8. Harmonic lattice by the perfectly matched multiscale simulations method: (a) $u(x, 50)$; (b) $u(x, 100)$; (c) $u(x, 130)$; (d) $u(x, 150)$.

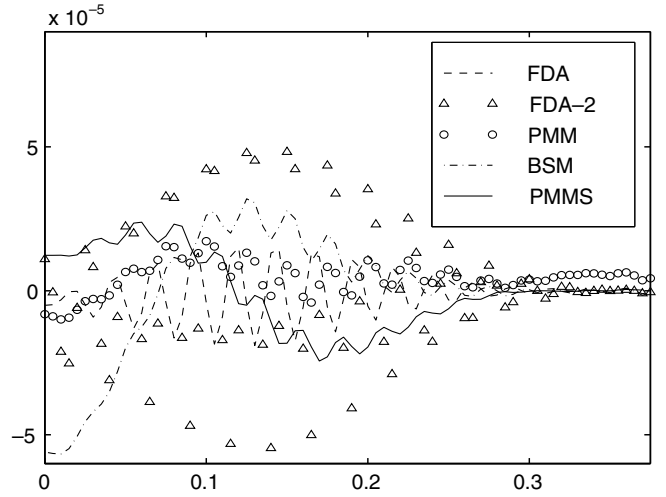

Fig. 9. Reflections in harmonic lattice at $t = 150$ by multiscale simulations: finite difference approach (dashed), finite difference approach with the second-order velocity interfacial condition (triangle), pseudo-spectral multiscale method (circle), bridging scale method (dash-dotted), and perfectly matched multiscale simulations (solid).

Snapshots for the simulations with $\overline{K} = 30$ are shown in Fig. 10 for the finite difference approach, in Fig. 11 for BSM, and in Fig. 12 for PMM, respectively. With the same initial profile as for the harmonic lattice, the long wave deforms by sharpening the gradient. The short wave also deforms. Furthermore, there is a certain amount of energy left in Ω_A when the major waves propagate away. From the figures, we observe that the finite difference approach treats well the nonlinearity, and the numerical solutions are indistinguishable from the exact solution in Ω_A. In contrast, numerical reflections appear for BSM and PMM when the short wave propagates out of Ω_A in the corresponding subplots (b) and (c), leaving a much higher energy in Ω_A afterwards in the corresponding subplots (d). The BSM solution outside of Ω_A deviates from the exact solution in terms of a kink ahead of the true wave, similar to the computation with harmonic

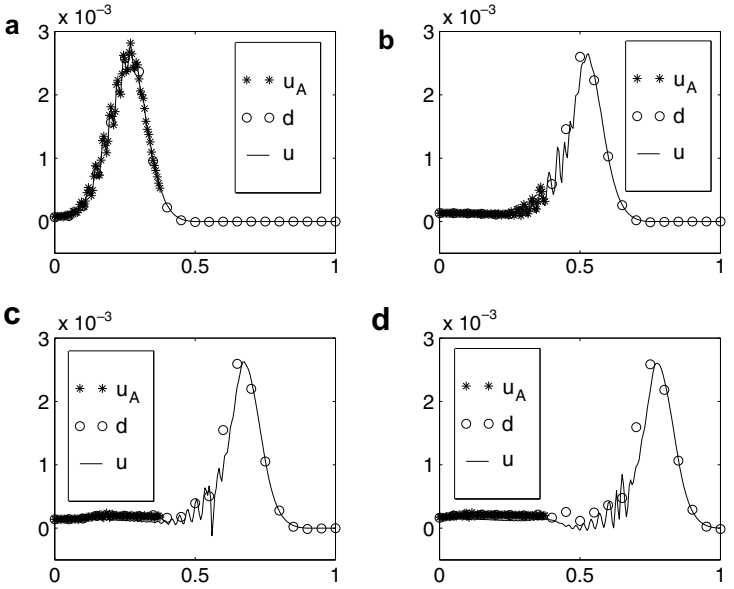

Fig. 10. Anharmonic lattice with $\overline{K} = 30$ by finite difference approach: (a) $u(x, 50)$; (b) $u(x, 100)$; (c) $u(x, 130)$; (d) $u(x, 150)$.

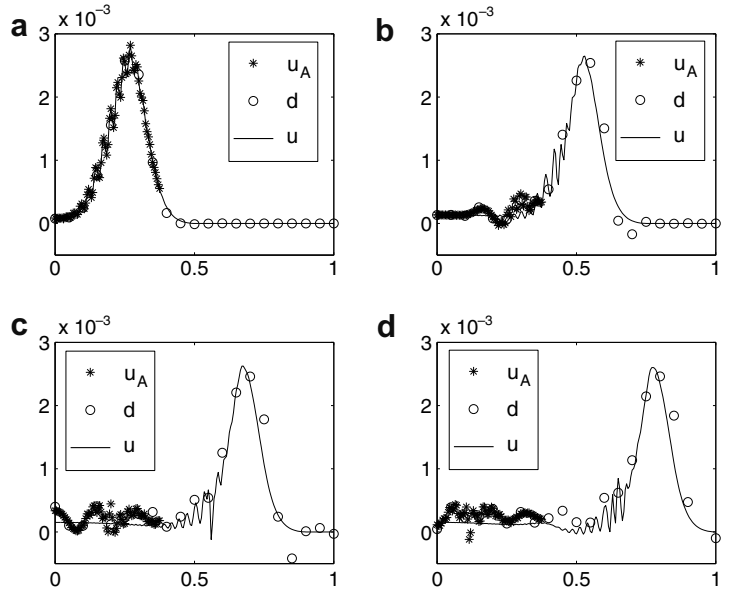

Fig. 11. Anharmonic lattice with $\overline{K} = 30$ by BSM: (a) $u(x, 50)$; (b) $u(x, 100)$; (c) $u(x, 130)$; (d) $u(x, 150)$.

lattice. Reflection at the interface is stronger than that in the PMM computation, as observed in subplots (b) and (c). In fact, both PMM and BSM adopt a time history kernel function corresponding to the harmonic lattice at equilibrium, generating large error in the stage when the nonlinear term dominates the evolution.

When we further increase the nonlinearity parameter to $\overline{K} = 50$, the difference between these methods increases. The nonlinearity is so strong that the coarse grid solution has an obvious phase delay in the tail of the long wave (see Fig. 13). The coarse grid solution near the interface is elevated in both BSM and PMM due to the reflection error in Ω_A, as displayed in subplots (c) and (d) of Figs. 14 and 15.

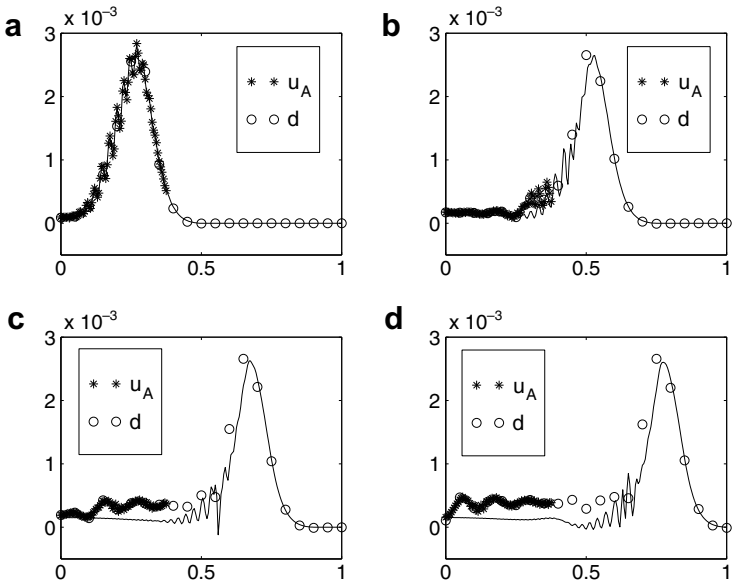

Fig. 12. Anharmonic lattice with $\overline{K} = 30$ by PMM: (a) $u(x, 50)$; (b) $u(x, 100)$; (c) $u(x, 130)$; (d) $u(x, 150)$.

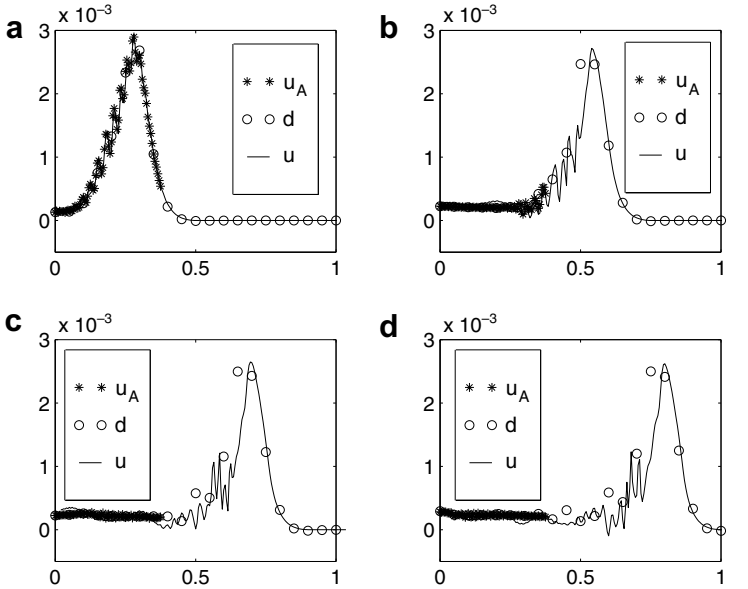

Fig. 13. Anharmonic lattice with $\overline{K} = 50$ by finite difference approach: (a) $u(x, 50)$; (b) $u(x, 100)$; (c) $u(x, 130)$; (d) $u(x, 150)$.

4.2.2. Lattice with the Lennard-Jones potential

The Lennard-Jones potential has wide applications. The strength of nonlinearity is related to the magnitude of the displacement.

We compute by the finite difference approach for two set of initial profiles in $\Omega = [-200r_0, 200r_0]$ with 41 coarse grid points ($p = 10$), and $\Omega_D = [-55r_0, 55r_0]$ with 111 atoms. The time step sizes are $\Delta\tau = 0.001$ and $\Delta t = 0.01$ for the fine and coarse scales, respectively.

The numerical results for initial data

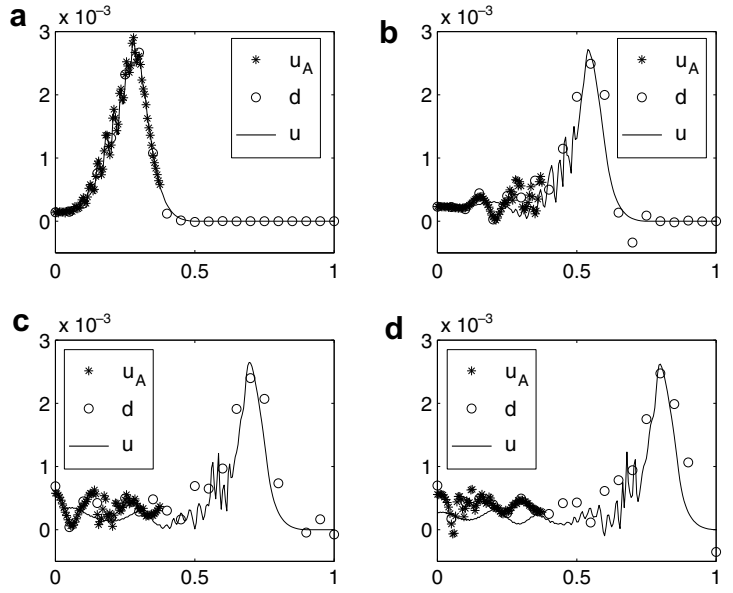

Fig. 14. Anharmonic lattice with $\overline{K} = 50$ by BSM: (a) $u(x, 50)$; (b) $u(x, 100)$; (c) $u(x, 130)$; (d) $u(x, 150)$.

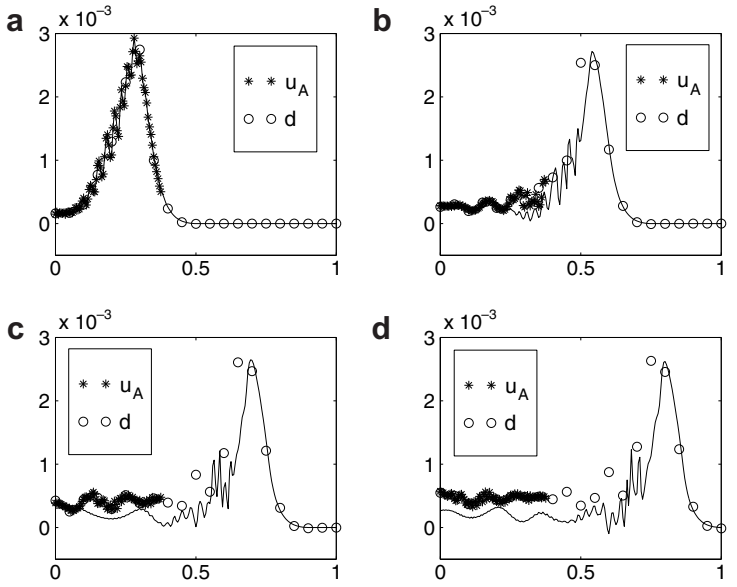

Fig. 15. Anharmonic lattice with $\overline{K} = 50$ by PMM: (a) $u(x, 50)$; (b) $u(x, 100)$; (c) $u(x, 130)$; (d) $u(x, 150)$.

$$u(x) = \begin{cases} 0.015\frac{e^{-(x/20)^2} - e^{-25}}{1 - e^{-25}}(1 + 0.2\cos(2\pi x/5)), & \text{if } |x| < 100, \\ 0, & \text{elsewhere}, \end{cases} \tag{58}$$

are depicted in Figs. 16 and 17. The multiscale computation agrees with the exact solution very well. Because the nonlinearity is not very strong for this setting, the performance of BSM is not much worse. Nevertheless, we notice obvious numerical error in Ω_B.

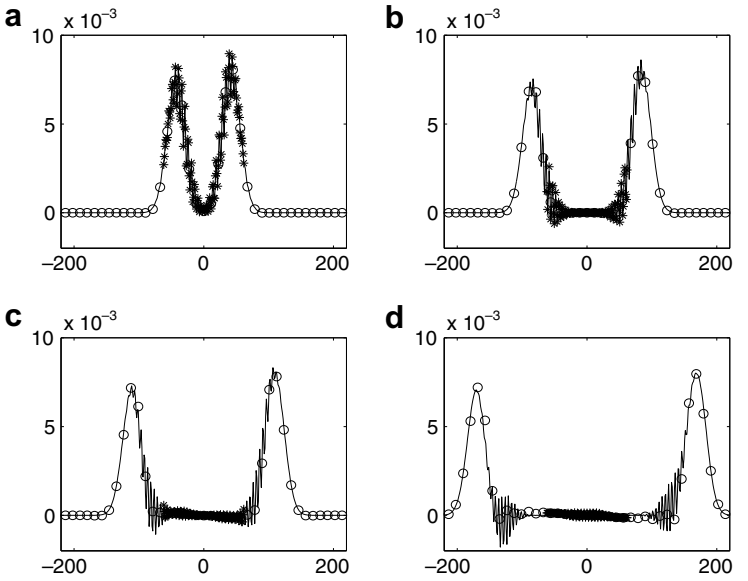

Fig. 16. Lattice with the Lennard-Jones potential by the finite difference approach (solid lines for the exact solution, stars and circles for the multiscale solution): (a) $u(x,5)$; (b) $u(x,10)$; (c) $u(x,13)$; (d) $u(x,20)$.

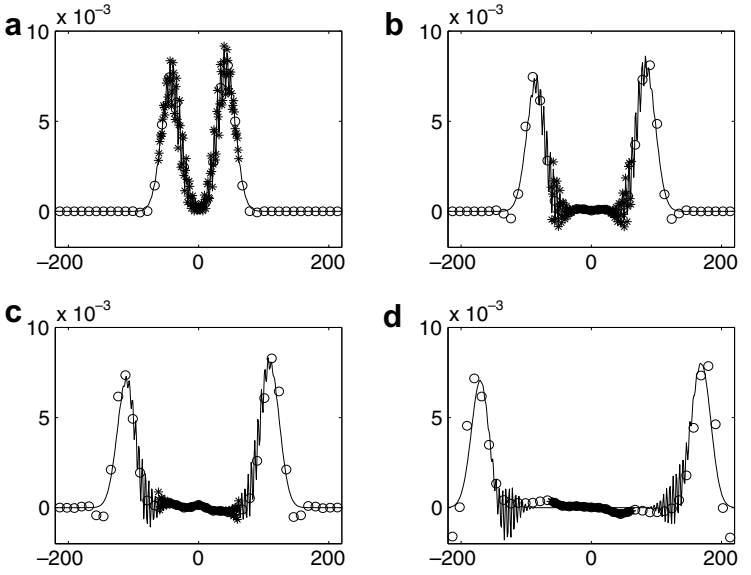

Fig. 17. Lattice with the Lennard-Jones potential by BSM (solid lines for the exact solution, stars and circles for the multiscale solution): (a) $u(x,5)$; (b) $u(x,10)$; (c) $u(x,13)$; (d) $u(x,20)$.

For an initial profile with a larger deformation, the nonlinearity increases. For instance, we compute with

$$u(x) = \begin{cases} 0.15\frac{e^{-(x/20)^2}-e^{-25}}{1-e^{-25}}(1+0.1\cos(2\pi x/5)), & \text{if } |x|<100, \\ 0, & \text{elsewhere.} \end{cases} \tag{59}$$

The numerical results in Fig. 18 still agree well with the exact solution. We remark that linear elasticity usually requires a strain below 1%. In this test, the strain is over 8%. In contrast, numerical results by BSM contain considerable wave reflection in Ω_A and inadequate resolution at coarse grid in Fig. 19.

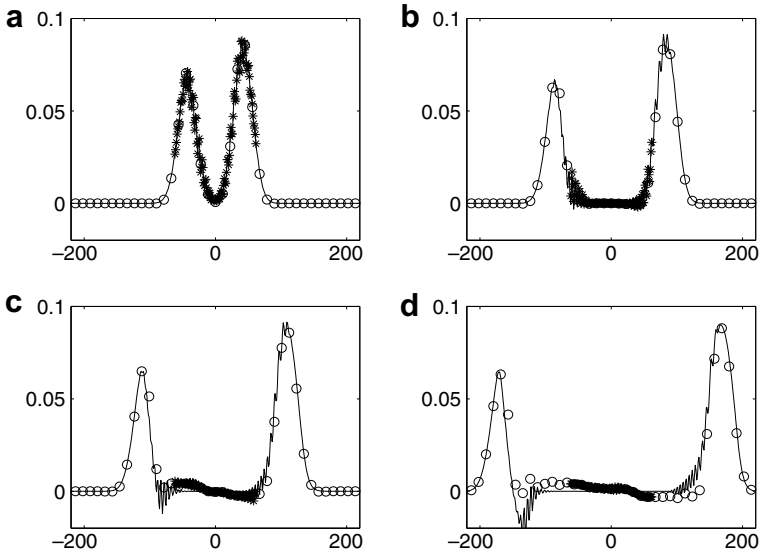

Fig. 18. Lattice with the Lennard-Jones potential by the finite difference approach (solid lines for the exact solution, stars and circles for the multiscale solution): (a) $u(x,5)$; (b) $u(x,10)$; (c) $u(x,13)$; (d) $u(x,20)$.

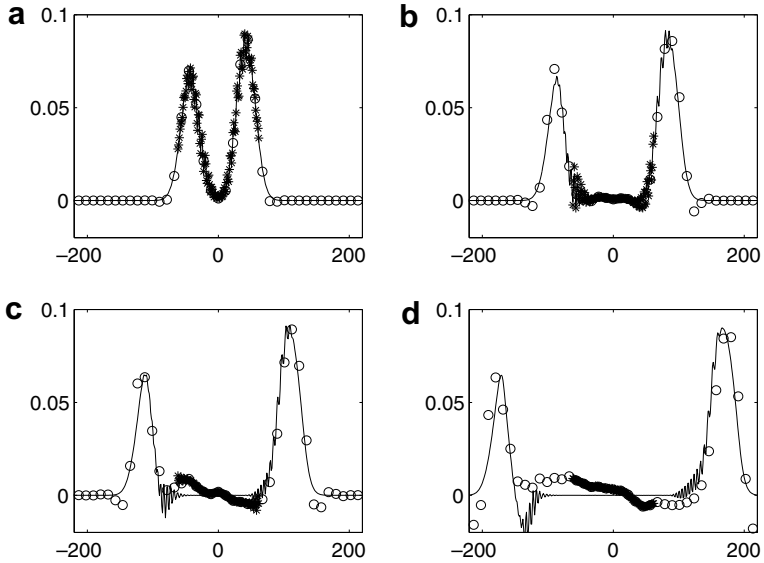

Fig. 19. Lattice with the Lennard-Jones potential by BSM (solid lines for the exact solution, stars and circles for the multiscale solution): (a) $u(x,5)$; (b) $u(x,10)$; (c) $u(x,13)$; (d) $u(x,20)$.

4.3. The Slepyan model for fracture in two space dimensions

We take a computing domain Ω with 257×513 atoms. The exact solution is computed by a full atomistic computation, with a time step size $\Delta\tau = 0.05$. Parameters include the damping coefficient $b = 0.01$, the coarsening ratios $p_x = p_y = 8$, $\Omega_A = [1,257] \times [178,335]$, and the coarse scale time step size $\Delta t = 0.5$.

We compute with an initial profile that contains a crack between the 256th and 257th layers, from the first atom to the 48th atom in the x-direction. The initial displacement and subsequent evolution are shown in Fig. 20.

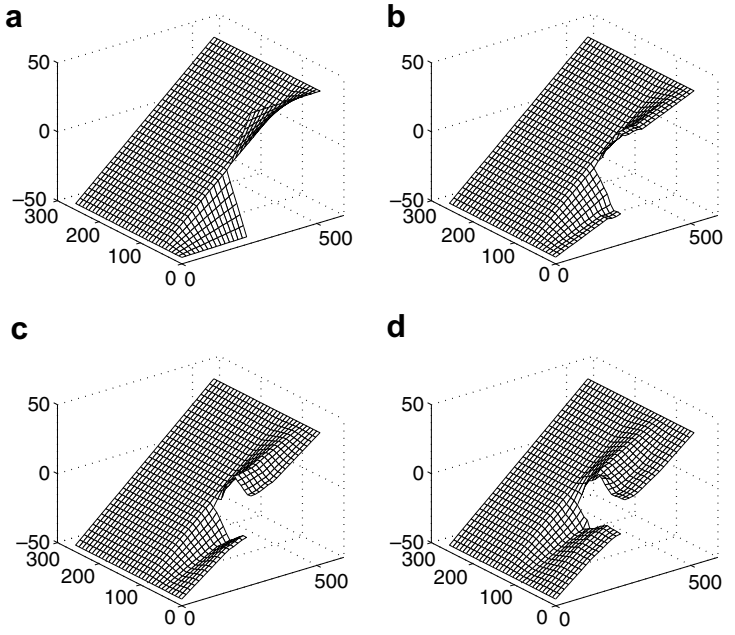

Fig. 20. Coarse grid displacement in Slepyan model: (a) $u(x,0)$; (b) $u(x,20)$; (c) $u(x,40)$; (d) $u(x,80)$.

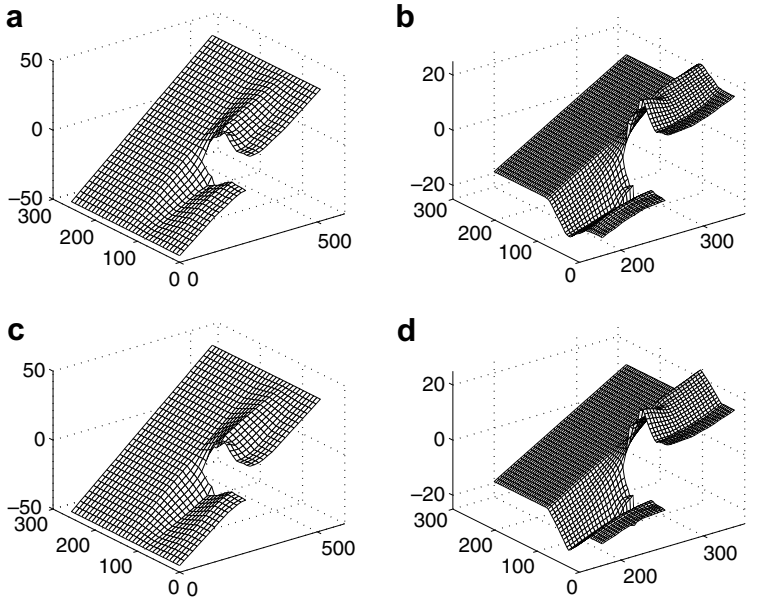

Fig. 21. Displacement in Slepyan model at $t = 80$: (a) coarse grid solution by the finite difference approach; (b) atomistic computation in Ω_A by the finite difference approach; (c) the exact solution; (d) the exact solution in Ω_A.

To compare the multiscale computation with the full atomistic solution, we display the two results at $t = 80$ in Fig. 21 for comparison. Differences in displacements are almost indiscernible, both in the coarse grid and in Ω_A. We remark that with such a thin strip for the atomistic region, the proposed method gives a convergent and accurate resolution for the fracture. On the other hand, it has been noticed that the bridging scale method may cause divergent results if the atomistic subdomain is not large enough [21].

5. Discussions

In this paper, we have proposed a finite difference approach for multiscale simulation of crystalline solids with relatively strong nonlinearity and large deformation. The controllable high accuracy in the coarse grid is reached with finite difference schemes, together with a fast averaging of the atomistic solution. The coarse grid algorithm efficiently captures the long wave dynamics.

In the atomistic subdomain, a class of velocity interfacial conditions have been proposed. Regarding the long waves as carriers for the fine fluctuations, we relate the velocities at several atoms near the interface to the atomistic displacement. The interfacial conditions describe the uni-directional wave propagation, hence enable the fluctuations to propagate out of Ω_A with the reflections effectively reduced. Moreover, the long waves determine the coefficient and propagation direction for the linearized uni-directional wave system. The formulation of the interfacial condition is local in both space and time, effective for nonlinear lattices and in multiple dimensions. We remark that the coarse grid schemes, the fast averaging technique, and the velocity interfacial conditions may be adopted separately. For instance, one may incorporate the velocity interfacial condition for the atomistic computation with an existing finite element code for the coarse grid continuum.

The overall approach is clear and simple, easy for implementation. With a low computing load, it reaches high balanced accuracy in both scales. For example, it is comparable to the much more expensive PMM in linear lattices.

There are various aspects for further explorations of the finite difference approach. In particular, we shall explore the application of the current method to dislocation dynamics with a phonon heat bath [29]. Applications to more general situations, such as fluid systems are also under consideration.

Acknowledgments

This research is partially supported by NSFC under Grant No. 90407021, National Basic Research Program of China under Contract Number 2007CB814800, and the China Ministry of Education under the NCETU Program. The author would like to acknowledge the anonymous referees for stimulating discussions, and Ms. Jun Xiao for reproducing the PMMS results.

Appendix. Matching differential operator method

Imagine that there is an intermediate continuous variable $z(x,t)$ for $x \in \Omega$. The atomistic displacement u and the coarse grid displacement d are regarded as discrete approximations to $z(x,t)$ with different resolutions, namely, $u_n(t) \approx z(x_n,t), d_J(t) \approx z(y_J,t)$. Let h_a be the atomistic spacing at rest, and the required order of accuracy be $o(h_a^l)$. If the atomistic dynamics (1) and the coarse grid scheme have the same modified equation in terms of $z(x,t)$ up to the order $o(h_a^l)$, we may expect that the consistency between u and an interpolation of d is on the same order. The coarse grid scheme is then called an MDO-l scheme for ease of presentation.

To be more precise, we perform the Taylor expansion to the displacement difference for two interacting atoms:

$$|u_i - u_n| = |z(x_i,t) - z(x_n,t)| = \left| \sum_{1 \leqslant |\alpha| \leqslant l} D^\alpha z(x_n,t) \frac{(x_i - x_n)^\alpha}{\alpha!} \right| + o(h_a^l). \tag{60}$$

Here the multiple index convention is used. Because only the displacement difference is involved in the potential U, we may perform the Taylor expansion to (2) and formally write the resulted modified equation

$$m(x) z_{tt} = \mathcal{K}_l(\nabla_x z) + o(h_a^l) \tag{61}$$

with $\mathcal{K}_l$ a nonlinear operator.

Selecting suitable functions and parameters, we may design a finite difference scheme on the coarse grid in terms of

$$\ddot{d} = A(d) \tag{62}$$

for which the Taylor expansion matches (61) to the same order of truncation error. The nonlinear vector function $A(d)$ is chosen to depend only on the coarse grid displacement differences in the form of $|d_I - d_J|$.

We notice that a delicate procedure has been proposed to coarsen the potential by using the Taylor expansion technique [3]. A coarse scale scheme may be designed using the coarsened potential. We further remark that the choice for $A(d)$ is not unique in general. Mathematical and physical intuitions are used to guide the design. A few examples are as follows.

In one space dimension, we let p be the coarsening ratio.

Harmonic lattice (8)

$$\ddot{d}_J = \mathcal{K}_{4,J} d \equiv \mathcal{K}_{2,J} d - \frac{p^2-1}{12p^4}(d_{J-2} - 4d_{J-1} + 6d_J - 4d_{J+1} + d_{J+2}). \tag{63}$$

Anharmonic lattice (33)

$$\begin{aligned}\ddot{d}_J = \mathcal{K}_{4,J} d + \frac{\overline{K}}{h_a^2 p^4}\left[(d_{J+1}-d_J)^3 - (d_J - d_{J-1})^3\right] - \frac{\overline{K}(p^2-1)}{4h_a^2 p^6}\cdot[(d_{J+1}-d_{J-1})^2(d_{J-2} - 4d_{J-1} + 6d_J \\ - 4d_{J+1} + d_{J+2})/4 + (d_{J-1} - 2d_J + d_{J+1})^3 + 2(d_{J+1} - d_{J-1})(d_{J-1} - 2d_J + d_{J+1})\cdot(-d_{J-3} \\ + 4d_{J-2} - 5d_{J-1} + 5d_{J+1} - 4d_{J+2} + d_{J+3})].\end{aligned} \tag{64}$$

Lattice with Lennard-Jones potential (36)

$$\begin{aligned}\ddot{d}_J = -\frac{48}{p}\left[\left(r_0 + \frac{d_{J+1}-d_J}{p}\right)^{-13} - \left(r_0 + \frac{d_J - d_{J-1}}{p}\right)^{-13}\right] \\ + \frac{24}{p}\left[\left(r_0 + \frac{d_{J+1}-d_J}{p}\right)^{-7} - \left(r_0 + \frac{d_J - d_{J-1}}{p}\right)^{-7}\right] + \frac{(p^2-1)(-52r_0^{-14} + 14r_0^{-8})}{p^4}(d_{J-2} - 4d_{J-1} \\ + 6d_J - 4d_{J+1} + d_{J+2}).\end{aligned} \tag{65}$$

In two space dimensions, we denote the coarsening ratios p_x and p_y in the x and y dimensions, respectively. For the Slepyan model (39), a coarse grid MDO-4 scheme reads

$$\begin{aligned}\ddot{d}_{IJ} = -b\dot{d}_{IJ} + \frac{1}{p_x^2}(d_{I-1,J} - 2d_{IJ} + d_{I+1,J}) + \frac{1}{p_y^2}(d_{I,J-1} - 2d_{IJ} + d_{I,J+1}) - \frac{p_x^2-1}{12p_x^4}(d_{I-2,J} - 4d_{I-1,J} \\ + 6d_{IJ} - 4d_{I+1,J} + d_{I+2,J}) - \frac{p_y^2-1}{12p_y^4}(d_{I,J-2} - 4d_{I,J-2} + 6d_{IJ} - 4d_{I,J+1} + d_{I,J+2}).\end{aligned} \tag{66}$$

We further remark that the MDO approach uses Taylor expansion to design coarse grid approximations for the atomistic Newton laws. This allows a direct application to more complex situations, such as non-nearest neighboring interaction, or multi-dimensional lattice structures. For an example, in a Lennard-Jones type of potential, we may make the following approximation with s an integer. A coarse grid scheme may be obtained by summing over terms in this form:

$$\begin{aligned}&(sr_0 + u_{n+s} - u_n)^{-k} - (sr_0 + u_n - u_{n-s})^{-k} \\ &\quad\approx s^{-(k-1)}\left\{\frac{1}{p}\left[\left(r_0 + \frac{d_{J+1}-d_J}{p}\right)^{-k} - \left(r_0 + \frac{d_J - d_{J-1}}{p}\right)^{-k}\right]\right. \\ &\quad\left. + \frac{kr_0^{-(k+1)}(p^2-s^2)}{12p^4}(d_{J-2} - 4d_{J-1} + 6d_J - 4d_{J+1} + d_{J+2})\right\}.\end{aligned} \tag{67}$$

References

[1] F.F. Abraham, J.Q. Broughton, N. Bernstein, E. Kaxiras, Spanning the continuum to quantum length scales in a dynamic simulation of brittle fracture, Europhys. Lett. 44 (1998) 783–787.

[2] S.A. Adelman, J.D. Doll, Generalized Langevin equation approach for atom/solid-surface scattering: collinear atom/harmonic chain model, J. Chem. Phys. 61 (1974) 4242–4245.

[3] M. Arndt, M. Griebel, Derivation of higher order gradient continuum models from atomistic models for crystalline solids, Multiscale Model. Simul. 4 (2005) 531–562.
[4] J.Q. Broughton, F.F. Abraham, N. Bernstein, E. Kaxiras, Concurrent coupling of length scales: methodology and application, Phys. Rev. B 60 (1999) 2391–2403.
[5] W. Cai, M. de Koning, V.V. Bulatov, S. Yip, Minimizing boundary reflections in coupled-domain simulations, Phys. Rev. Lett. 85 (2000) 3213–3216.
[6] J. Dolbow, M.A. Khaleel, J. Mitchell, Multiscale mathematics initiative: a roadmap, DOE report, 2004.
[7] W. E, Z. Huang, A dynamic atomistic-continuum method for simulation of crystalline materials, J. Comput. Phys. 182 (2002) 234–261.
[8] B. Engquist, A. Majda, Radiation boundary conditions for acoustic and elastic calculations, Commun. Pure Appl. Anal. 32 (1979) 313–357.
[9] D. Givoli, J.B. Keller, Non-reflecting boundary conditions for elastic waves, Wave Motion 12 (1990) 261–279.
[10] M.J. Grote, J.B. Keller, Nonreflecting boundary conditions for time-dependent scattering, J. Comput. Phys. 127 (1996) 52–65.
[11] R.L. Higdon, Radiation boundary conditions for dispersive waves, SIAM J. Numer. Anal. 31 (1994) 64–100.
[12] E. Karpov, H. Park, W. Liu, A phonon heat bath approach for the atomistic and multiscale simulation of solids, Int. J. Numer. Methods Eng. 70 (2007) 351–378.
[13] E. Karpov, G. Wagner, W. Liu, A Greens function approach to deriving nonreflecting boundary conditions in molecular dynamics simulations, Int. J. Numer. Methods Eng. 62 (2005) 1250–1262.
[14] S. Kohlhoff, P. Gumbsch, H.F. Fischmeister, Crack propagation in BCC crystals studied with a combined finite element and atomistic model, Philos. Mag. A 64 (1991) 851–878.
[15] X. Li, W. E, Variational boundary conditions for molecular dynamics simulations of solids at low temperature, Commun. Comput. Phys. 1 (2006) 136–176.
[16] W.K. Liu, E.G. Karpov, H.S. Park, Nano-Mechanics and Materials: Theory, Multiscale Methods and Applications, Wiley, 2005.
[17] R.E. Miller, E.B. Tadmor, The quasicontinuum method overview applications and current directions, J. Comput.-Aided Mater. Des. 9 (2002) 203239.
[18] X.B. Nie, M.O. Robbins, S.Y. Chen, Resolving singular forces in cavity flow: multiscale modeling from atomic to millimeter scales, Phys. Rev. Lett. 96 (2006) 134501.
[19] S.T. O'Connell, P.A. Thompson, Molecular dynamics-continuum hybrid computations: a tool for studying complex fluid flows, Phys. Rev. E 52 (1995) R5792–R5795.
[20] M. Ortiz, Continuum models of dislocation dynamics and dislocation structures, in: Gordon Research Conference on Physical Metallurgy, Plymouth, NH, 2004.
[21] H.S. Park, E.G. Karpov, W.K. Liu, P.A. Klein, The bridging scale for two-dimensional atomistic/continuum coupling, Philos. Mag. A 85 (2005) 79–113.
[22] H. Park, E. Karpov, P. Klein, W. Liu, Three-dimensional bridging scale analysis of dynamic fracture, J. Comput. Phys. 207 (2005) 588–609.
[23] D. Qian, G.J. Wagner, W.K. Liu, A multiscale projection method for the analysis of carbon nanotubes, Comput. Methods Appl. Mech. Eng. 193 (2004) 1603–1632.
[24] R.E. Rudd, J.Q. Broughton, Concurrent coupling of length scales in solid state systems, Phys. Status Solidi 217 (2000) 251–291.
[25] L.I. Slepyan, M.V. Ayzenberg-Stepanenko, J.P. Dempsey, A lattice model for viscoelastic fracture, Mech. Time-dependent Mater. 3 (1999) 159–203.
[26] E.B. Tadmor, M. Ortiz, R. Phillips, Quasicontinuum analysis of defects in solids, Philos. Mag. A 73 (1996) 1529–1563.
[27] S. Tang, T.Y. Hou, W.K. Liu, A mathematical framework of the bridging scale method, Int. J. Numer. Methods Eng. 65 (2006) 1688–1713.
[28] S. Tang, T.Y. Hou, W.K. Liu, A pseudo-spectral multiscale method: interfacial conditions and coarse grid equations, J. Comput. Phys. 213 (2006) 57–85.
[29] S. Tang, W.K. Liu, E.G. Karpov, T.Y. Hou, Bridging atomistic/continuum scales in solids with moving dislocations, Chin. Phys. Lett. 24 (2007) 161–164.
[30] A.C. To, S. Li, Perfectly matched multiscale simulations, Phys. Rev. B 72 (2005) 035414.
[31] G.J. Wagner, W.K. Liu, Coupling of atomistic and continuum simulations using a bridging scale decomposition, J. Comput. Phys. 190 (2003) 249–274.
[32] J. Xiao, A new approach for multiscale computations in crystalline systems, M.Phil. Thesis, Peking University, Beijing, 2006.